Journal of Power Sources 594 (2024) 234022

Contents lists available at ScienceDirect

Journal of Power Sources

journal homepage: www.elsevier.com/locate/jpowsour

Cyclic-induced deformation and the degradation of Al-doped LLZO electrolytes in all-solid-state Li-metal batteries

John Adjah [a,c], Kingsley I. Orisekeh [b], Ridwan A. Ahmed [c], Mobin Vandadi [e], Benjamin Agyei-Tuffour [a,**], David Dodoo-Arhin [a], Emmanuel Nyankson [a], Joseph Asare [f], Nima Rahbar [c,e], Winston O. Soboyejo [c,d,*]

[a] Department of Materials Science and Engineering, School of Engineering Sciences, College of Basic and Applied Sciences, University of Ghana, Legon, Accra, Ghana
[b] National Space Research and Development Agency (NASRDA), Airport Road, Abuja, Federal Capital Territory, Nigeria
[c] Department of Mechanical Engineering, Program in Materials Science and Engineering, Worcester Polytechnic Institute, Worcester, MA, 01609, USA
[d] State University of New York Polytechnic Institute, College of Engineering, 100 Seymour Rd, Utica, NY, 13502, USA
[e] Department of Civil and Environmental Engineering, Worcester Polytechnic Institute, Worcester, MA, 01609, USA
[f] Department of Physics, School of Physical and Mathematical Sciences, College of Basic and Applied Sciences, University of Ghana, Legon, Accra, Ghana

HIGHLIGHTS

- SEM images of Cyclic-induced strains and crack propagation in solid LLZO electrolyte.
- Numerical simulation of Joule heating induced stress-strain ranges (eigenstrains).
- Strain measurements using Digital Image Correlation (DIC) techniques.
- Effects of charge-discharge on capacity and ionic conductivity.

ARTICLE INFO

Keywords:
All-solid-state Li-Ion batteries
Al-doped LLZO
Stress/strain state
Impedance
Electrochemical degradation
Charge-discharge cycles
Ionic conductivity

ABSTRACT

This paper presents the results of a study of the mechanical degradation of Li-oxide garnet solid electrolyte, $Li_7La_3Zr_2O_{12}$ (LLZO) in all-solid-state lithium metal batteries. A coupled thermo-electro-chemo-mechanical model was used to analyze stress-strain distribution and cracking phenomena within the electrolyte. A combination of in-situ/ex-situ microscopic observations, strain mapping and finite element modeling were deployed to study the progressive deformation and cracking phenomena that occur as a result of electrochemical charging and discharging, thermal runaway, and joule heating phenomenon. The results show that strains induced during discharge cycles are more significant than those induced during charging phase. The accumulation of strains during charging and discharging is also shown to result ultimately in cracking that impedes Li ion transport, while accelerated electro-chemical degradation. The implications of these processes are discussed for the development of robust and durable all-solid-state batteries.

1. Introduction

Rechargeable lithium-ion batteries (LIBs) have attracted significant research interest in recent years. This is because of the increased demand for portable electronic devices such as mobile phones, camcorders, laptops, notebook computers and the integration of electric vehicles (EVs) into the transportation mix [1–4]. However, the existing commercialized Li-ion batteries (LIBs) contain liquid and polymer-supported electrolytes with undesirable properties. These include dendrite formation [5], leakages [6], and flammability [7,8]. This has serious safety implications that need to be addressed. Hence, there is a need for the next generation and robust, safer, and nonflammable batteries. Solid-state fast Li-ion conductors have emerged as the most feasible alternative to conventional liquid-based electrolyte LIBs

* Corresponding author. College of Engineering, SUNY Polytechnic Institute, Utica, NY, 13502, USA.
** Corresponding author. Department of Materials Science and Engineering, Off Anne Jiaggi Road, School of Engineering Sciences, College of Basic and Applied Sciences, University of Ghana, Legon, Accra, Ghana.
E-mail addresses: bagyei-tuffour@ug.edu.gh (B. Agyei-Tuffour), soboyew@sunypoly.edu (W.O. Soboyejo).

https://doi.org/10.1016/j.jpowsour.2023.234022
Received 31 October 2023; Received in revised form 7 December 2023; Accepted 26 December 2023
Available online 30 December 2023

Table 1
Summary of ion and electron transport in both electrodes through the electrolyte during electrochemical cycling [38].

Electrode	Charging	Discharging	Process
Cathode (+ve)	Intercalation	Deintercalation	Ionic
	Reduction	Oxidation	Electronic
Anode (-ve)	Stripping	Electrodeposition/plating	Ionic
	Oxidation	Reduction	Electronic

[6,7]. All-solid-state Li-ion batteries (ASSLBs) have the potential to overcome the physicochemical limits of commercialized liquid-based Li-ion batteries [5,7,8]. Furthermore, most ASSLB have superior energy and power densities, rate capability, thermal stability and intrinsically safer [9–13].

Prior research studies by Murugan et al., 2007 [7], Sastre et al., 2020 [5] and Thangadurai et al., 2003 [7] have shown that Li-oxide garnets exhibit high ionic conductivities, stable chemical, and physical properties to be used as potential electrolytes in ASSLBs. However, among the Li-oxide garnets, $Li_7La_3Zr_2O_{12}$ (LLZO) possesses superior Li-ion conductivities and wide electrochemical stability window ((~0 – 6 V) against Li metal anode [5,6,14–16]. This makes LLZO material the most promising solid electrolyte candidate in ASSLBs. Additionally, earlier studies have demonstrated that LLZO can exist in different crystalline polymorphs. At room temperature, pure LLZO exists as tetragonal phase (space group $I4_1/acd$) with limited ionic conductivities (~10^{-6} Scm^{-1}) [5]. However, LLZO undergoes phase transformation into high-temperature cubic phase (space group Ia $\bar{3}$ d) with superior ionic conductivities ranging ((~10^{-3} – 10^{-4})Scm^{-1}) at room temperature [6,7]. The disparity in ionic conductivity primarily arises from the distinct ion transport mechanisms present in each crystalline polymorph [17]. The cubic phase contains many vacancies in Li sites, facilitating ion movement along a clearly defined pathway. The mechanisms of ion movement in the cubic phase require less activation energy compared to the ionic movement in the tetragonal phase [6,17,18]. Furthermore, introducing aliovalent dopants (e.g. Al^{3+}, Ga^{3+}) into LLZO at room temperature holds the potential to stabilize the cubic phase at elevated temperature [5,6]. The aliovalent dopants normally substitute the Li sites inducing further vacancies and influence the density and current density of the electrolyte [5].

Despite these intriguing characteristics, ASSLBs still encounter various unresolved challenges that render them unreliable and difficult to commercialize. These issues stem largely from the significant interfacial resistance between the solid-state electrolytes (SSEs) and the electrodes [17,19–21].

In the context of solid-state Li metal batteries, the occurrence of thermal runaway [22] and joule heating in solid electrolytes, exemplified by LLZO, arises from applying high voltage, generating a substantial electric field and current density [23–26]. This occurrence adversely affects the structural integrity of LLZO, leading to thermal expansion, phase transformation, and alterations to the microstructure [27,28]. Furthermore, the phenomena of thermal runaway and joule heating can induce the shift from the high-conductivity cubic phase to the low-conductivity tetragonal phase [24,29]. This leads to a reduction in ionic conductivity and an increase in internal resistance [27]. Additionally, it has the potential to induce grain growth, cracking, and delamination of the electrolyte, resulting in compromised mechanical properties and interfacial stability [30,31].

Throughout electrochemical cycling in all-solid-state lithium batteries, the recurrent insertion and extraction sequence of lithium ions into and from electrodes adversely affect the structural integrity of the LLZO electrolyte [24]. This process induces interfacial reactions, stress

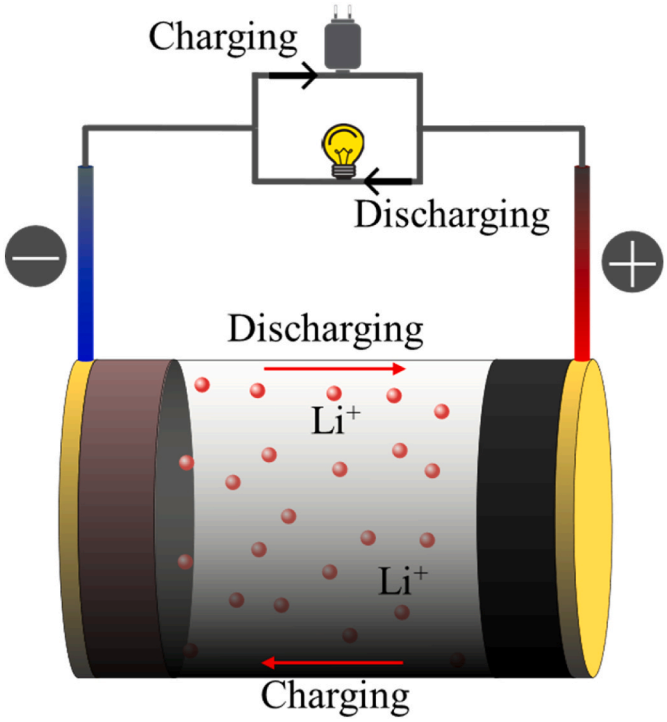

Fig. 2. Schematic diagram of electrochemical measurements.

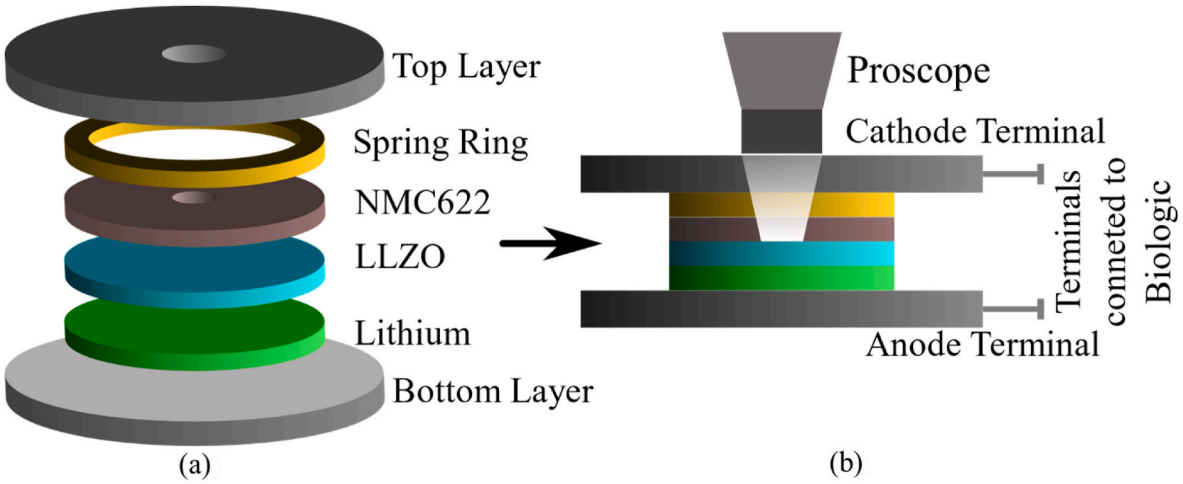

Fig. 1. Schematic diagram of (a) assembling cell components (b) electrochemical cycling test using split test cell.

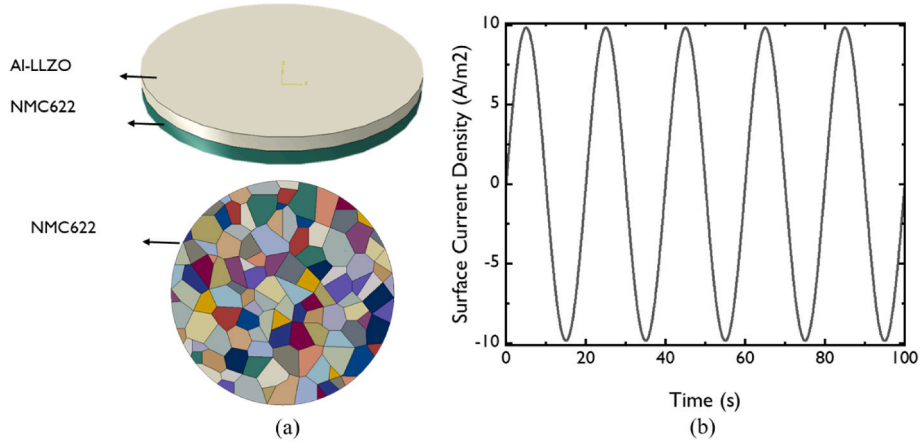

Fig. 3. (a) The system modeled for numerical analysis of the charge and discharge process. Top image is the system for the initial step and the image below is the polycrystal image for the crack propagation step, (b) Surface current change during the simulation.

Table 2
Properties of Al-LLZO and NMC622 layers used in numerical modeling.

Material	Young's Modulus (GPa)	Poisson Ratio (–)	Yield Stress (MPa)	Specific Heat ($Jkg^{-1}{}^{\circ}C^{-1}$)	Electrical Conductivity (Sm^{-1})	Dielectric Constant (Cm^{-1})	Heat Conductivity ($Wm^{-1}K^{-1}$)	Thermal Expansion (K^{-1})
Al-LLZO	8.83	0.26	14.75 [48]	738.86 [49]	1.85×10^{-2} [50]	50 [51]	0.5 [52]	1.55×10^{-5} [53]
NMC622	7.21	0.10	47.34 [54]	1010 [55]	1×10^{-1} [56]	36.224 [57]	1.38 [58]	1.20×10^{-4} [59]

Table 3
The theoretical, actual, and relative densities of undoped and Al-doped LLZO pellet.

Material	Theoretical density/ gcm^{-3}	Actual density/ gcm^{-3}	Relative density/%
Undoped-LLZO	5.110	4.264	83.44
Al-doped LLZO	5.110	4.973	97.32

accumulation, and chemical degradation [9,32]. Interfacial layers, such as the solid electrolyte interphase (SEI) and cathode-electrolyte interphase (CEI), form, leading to modifications in the electrolyte's chemical composition, morphology, and mechanical properties [24]. Stress accumulation during charge-discharge cycles, driven by volumetric changes in electrodes and lithium plating/stripping at the anode, increases the risk of cracking, fracture, and detachment of the electrolyte [6,33].

For solid lithium metal batteries, the localized stretching and shearing effects could be a consequence of particle mismatches, changes in volume during charging and discharging cycles, or uneven surfaces. These effects can impact the structural integrity of the battery components and may lead to issues such as mechanical stress, deformation, or even failure in specific regions rather than uniformly across the entire material [30,31,34–37].

In this work, to gain insight into the challenges, we employed a combination of experimental (in-situ/ex-situ microscopic observations, Digital Imaging Correlation, SEM-EDS, XRD and Electrochemical Impedance Spectroscopy) techniques and finite element modeling to study the stress-strain evolution, cracking/fracture, and deformation that occur because of thermo-electro-chemo-mechanical coupling in ASSLBs. Understanding and mitigating these intricate couplings between temperature variability, electrochemical processes, mechanical stresses, and chemical interactions is crucial for designing robust and durable all-solid-state lithium batteries.

2. Theory

2.1. Electrochemistry

Rechargeable batteries facilitate reversible chemical reactions at both anode and cathode electrodes. The two primary types of reversible electrochemical reactions at solid electrodes within All-Solid-State Batteries (ASSBs) are displacement and insertion reactions [38–40]. Intercalation reactions transpire at the solid cathode electrode (Eqn. (1)), while the stripping of Li metal occurs at the solid anode (see Eqn. (2)) [41]. The electrodes that undergo intercalation reactions are composed of ionically and electronically conductive host materials, into which the working ion (e.g., Li^+-ion) can be reversibly intercalated or extracted. The application of potential across the electrodes propels Li-ions across the electrolyte from the cathode to the anode during the charging phase. A charge potential also emerges between the electrolyte and the electrode as ions become intercalated within the voids of the cathode composite structure [41,42].

During the discharge process, the electroactive species of the cathode material experience depletion, leading to the intercalation of Li + ions into the lattice of the host material [42,43]. Discharge-driven intercalation occurs by spontaneous redox reactions occurring at the electrode surface. Electroneutrality is maintained by the flow of electrons across the external circuit connecting the negatively charged anode to the positively charged cathode. As illustrated in Fig. 2, ions and electrons are subsequently directed back into the negative electrode and electrodeposited at the Li metal electrode during the battery's charging phase, prompted by an external load (Table 1) [38]. The electrochemical reactions intrinsic to the charging-discharging mechanism in the Li metal battery are governed by Eqn. (1), Eqn. (2) and Eqn. (3) [14,15,32,38,40,44]:

Cathodic half reaction equation:

$$LiMO_2 \rightleftharpoons Li_{1-x}MO_2 + xLi^+ + xe^- \quad (0 \le x \le 0.5) \qquad \text{Eqn. 1}$$

(M = Transition metals, e.g., Mn, Ni, Co, etc.)

Anodic half reaction equation:

$$Li \rightleftharpoons Li_{1-x} + xLi^+ + xe^- \qquad \text{Eqn. 2}$$

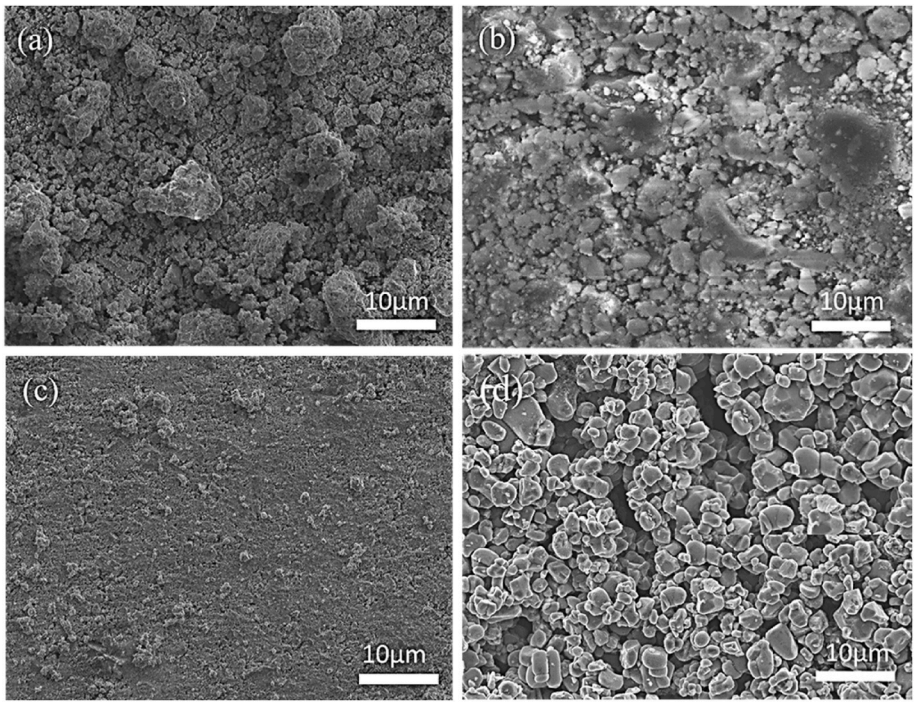

Fig. 4. SEM image of (a) LLZO powder (b) undoped LLZO pellet (c) Al-doped LLZO pellet and (d) NMC 622.

Overall reaction equation:

$$LiMO_2 + Li_{1-x} \rightleftharpoons Li_{1-x}MO_2 + Li \quad \text{Eqn. 3}$$

2.2. Electrochemical cyclic deformation and cracking phenomenon

Mechano-electrochemical cracking occurs within solid-state electrolytes (SSEs) during battery operation [45]. These can be attributed to the effects of electrochemical cycling, which leads to the migration of lithium ions across solid electrolytes. This generates thermal shocks and instigates the evolution of strains within the electrolyte [37,41]. Additionally, the transportation of ions through the electrolyte (during charge-discharge processes) contributes to the accumulation of strain within the electrolyte. Such strain accumulation results in cyclic damage via plastic deformation and microcracking, ultimately the degradation of battery performance.

3. Materials and methods

3.1. Preparation of electrolyte and positive electrode

The synthesis of lithium lanthanum zirconate, Li7La3Zr2O12 (LLZO), with a 3 wt% Al2O3 doping (to stabilize the cubic phase) was conducted in a three-step solid-state reaction under an argon atmosphere. The precursor powders, Li2CO3 (99.0 %), La2O3 (99.99 %), and ZrO2 (99.98 %), were obtained from Sigma Aldrich, St. Louis, MO, USA. These powders were blended in a molar ratio of 7:3:2 (Li7La3Zr2O12). To compensate for the loss of Li during calcination, an excess of 10 wt% Li2CO3 was incorporated. The Al-doped LLZO powders were prepared by ball-milling the precursor mixture in planetary ball-milling equipment (PQ-N04 Gear-Drive 0.4-L Planetary Ball Mills, 4 × 100 m, Across International, Livingston, NJ 07039, USA) at 600 rpm for 12 h to achieve a fine powder. Subsequently, the mixture was calcined using (Lindberg Blue M, Thermo Fisher Scientific 1100 °C Box Furnace BF51800 Series, Asheville, NC, USA) at 1000 °C for 12 h. The calcined material was then subjected to further ball-milling and cold pressing into pellets of 0.80 mm thickness using a force of 20 kN for 15 min, using an Instron 8872 servo-hydraulic system (Norwood, Massachusetts, USA). Furthermore, the pellets were sintered at 500 °C for 12 h.

The actual and relative densities were computed to assess the compactness of the cylindrical LLZO pellet (see Table 3). Actual density was calculated by weighing the mass of pellet and dividing it by the calculated volume, then compared to the density obtained from XRD. High relative density confirms synthesis quality, crystal structure, and uniformity, offering crucial insights into the electrochemical and mechanical properties of the LLZO electrolyte.

The positive electrode was prepared through a sequential process. Initially, polyvinylidene fluoride (PVDF) was dissolved in N-methyl pyrrolidone (NMP) as a binder at a concentration of 5 wt%. Subsequently, NMC622 (91 wt%) and Super P Conductive Carbon Black (4 wt %) were added to the solution to enhance electronic conductivity within the electrode and lithium-ion battery performance. The resulting mixture was stirred using a magnetic stirrer to create a slurry. The slurry was then applied onto an aluminum foil substrate using a cast coater (Mini Tape Casting Coater MSK-AFA-HC100 from MTI Corporation, Richmond, CA, USA). Following this, the electrode film was subjected to drying in a vacuum oven at 80 °C for 12 h to remove NMP. The dried film was subsequently shaped into circular discs using a disk cutter (Pneumatic Disk Cutter MSK-180SC from MTI Corporation, Richmond, CA, USA). To obtain the active cathode electrode material, the circular disc electrodes were further dried at 120 °C for 12 h within an argon-filled glovebox.

3.2. Physicochemical characterizations

The microstructure of the solid electrolyte (LLZO/Al-LLZO) and the synthesized positive electrode (NMC622) were examined using a scanning electron microscope (SEM) (JEOL, JSM-700F Field Emission Scanning Electron Microscope, Tokyo, Japan). The elemental distribution in both the cathode and electrolyte were also characterized using energy dispersive spectroscopy during scanning microscopy (SEM-EDS) (JEOL, JSM-700F Field Emission Scanning Electron Microscope, Tokyo, Japan). An in-situ electrochemical cell was also designed and used to monitor the surface of the Al-LLZO electrolyte during electrochemical cycling.

The structure of the LLZO powder and NMC622 was characterized

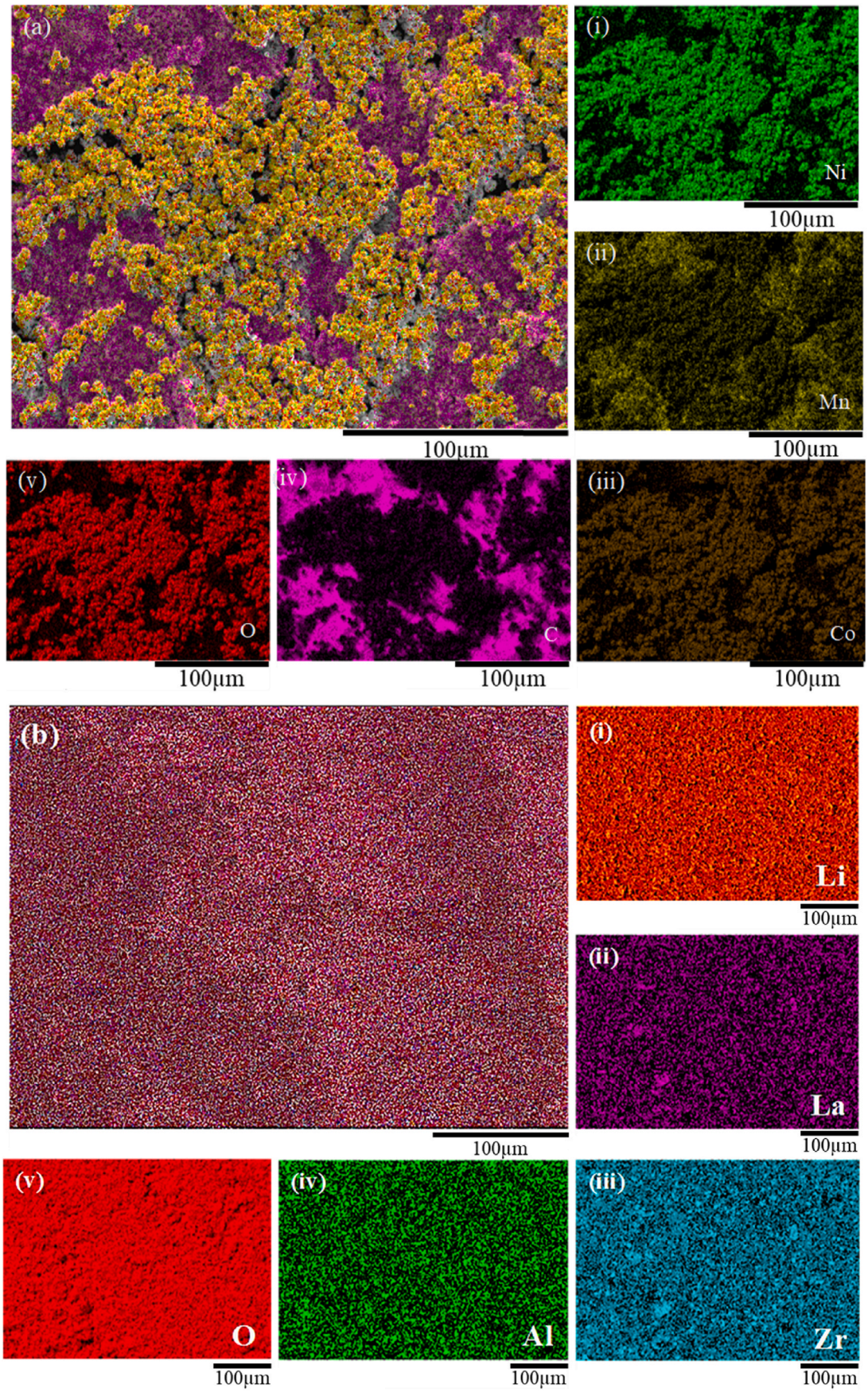

Fig. 5. a (i–v) SEM-EDS image of NMC 622-based electrode and b (vi - xii) SEM-EDS maps of Al-LLZO electrolyte.

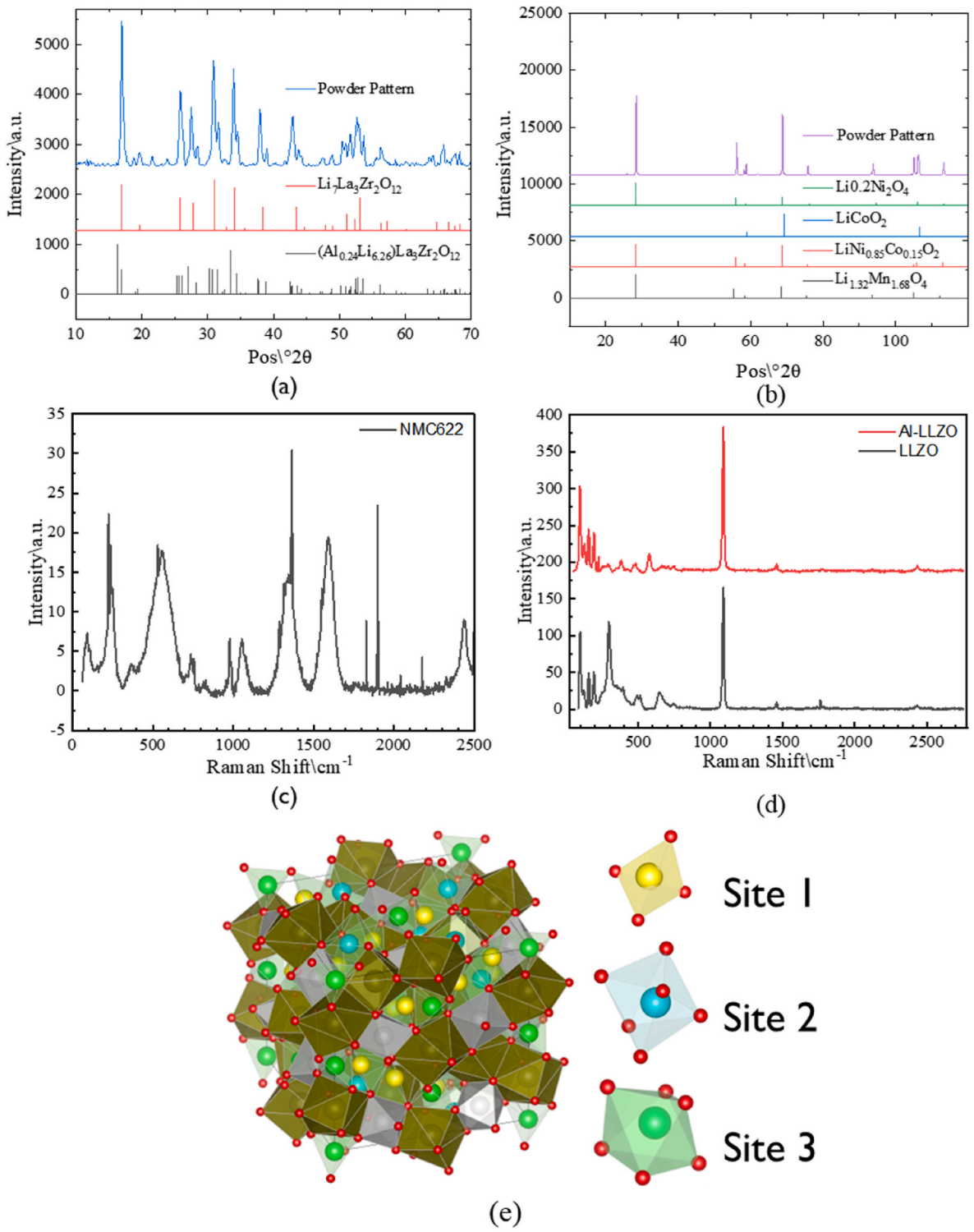

Fig. 6. Shows X-ray diffraction pattern for: (a) Al-LLZO and pure LLZO (b) NMC622 electrode, and Raman Spectra for: (c) NMC622 (d) Al-LLZO and LLZO for phase analysis, (*e*) Crystal structure model for cubic Al-LLZO and the lithium sites in the system *(refer to* Table 5).

using Raman Spectroscopy (Horiba Xplora Raman System) instrumented with a solid-state 532 nm excitation laser and a 1200 mm^{-1} grating. The laser power output was deliberately limited to 25 % to prevent any material degradation. The crystalline phases present (in both the LLZO and NMC622 electrode materials) were characterized with XRD. The XRD patterns were acquired from an X-ray diffractometer (Rigatu, Smart Lab, Tokyo, Japan) (PANalytical) across a diffraction angle range of 10°–90°, utilizing Cr Kα X-rays (1.5406 Å at 30 kV and 55 mA).

3.3. Cell assembly

Li||NMC622 cells were assembled using an in-situ analytical split test cell set up as illustrated in Fig. 1, with Al-LLZO serving as both the separator and solid-state electrolyte. The split test cell is equipped with quartz observation window (φ 9.3 mm × 1.92 mm thick and recessed area of 6 mm) to allow for infrared beam penetration and a two protruding terminal pins which are connected to Biologic SP-300

Table 4
Lattice parameters of pure LLZO, Al-LLZO and NMC622 were obtained from the HighScore Plus Rietveld refinement of XRD data.

Phase	Unit cell volume ($Å^3$)	Space group	$a[Å]$	$b[Å]$	$c[Å]$
$(Li_{6.26}Al_{0.24})La_3Zr_2O_{12}$	2178.44	Ia $\bar{3}$ d	12.963	12.963	12.963
$Li_7La_3Zr_2O_{12}$	2166.89	I41/acd	13.107	13.107	12.614
$LiNi_{0.85}Co_{0.15}O_2$	101.04	R $\bar{3}$ m	2.870	2.870	14.169
$Li_{0.20}Ni_2O_4$	531.83	Fd $\bar{3}$ m	8.102	8.102	8.102
$Li_{1.32}Mn_{1.68}O_4$	543.66	Fd $\bar{3}$ m	8.162	8.162	8.162
$(LiCo)O_2$	65.79	Fm $\bar{3}$ m	4.037	4.037	4.037

Potentiostat for measurement. A spring, NMC622 (with a small circular disc hole punched at the center to allow for real-time video recordings of the surface deformation during charge-discharge cycles), the electrolyte, Li metal chip and stainless-steel disc (serving as electrical contact) were assembled and tightened inside the split test cell. This set-up allows for an *in-situ* measurement of the mechanical deformation of the electrolyte surface during electrochemical cycling which will be discussed in detail in the stress -strain measurement section.

3.4. Electrochemical testing

This study encompassed the investigation of the electrochemical impedance spectroscopy (EIS) of the cell within the frequency range of 7 MHz to 0.1Hz, at an elevated temperature of 60 °C, utilizing the Bio-Logic SP-300 potentiostat (BioLogic, Seyssinet-Pariset, Auvergne-Rhone-Alpe, France). A perturbation amplitude of 10 mV was used. The galvanostatic cycling of the cell was conducted at a rate of 0.5 C, encompassing a voltage window spanning from 2.8 V to 4.2 V. The conductivities of the cells were computed by evaluating the bulk resistance at 60 °C, extracted by fitting the EIS data to the equivalent circuit model incorporated within the EC-Lab software (BioLogic, Seyssinet-Pariset, Auvergne-Rhone-Alpe, France), as indicated by Eqn. (4) [44,46,47]. Fig. 2 provides an illustrative schematic of the electrochemical cycling process.

$$\sigma \Big/ \mathrm{Scm}^{-1} = \frac{l}{R1_{bulk} \times A} \qquad \text{Eqn. 4}$$

where σ/Scm^{-1} represents the ionic conductivity of the electrolyte, $R1_{bulk}$ signifies the bulk resistance, ℓ denotes the thickness of the electrolyte, and An indicates the cross-sectional area of the electrolyte.

3.5. Stress-strain measurements

The evaluation of stress-strain evolution within the electrolyte was conducted utilizing the digital imaging correlation (DIC) technique. Initially, a small circular disc hole was created at the center of the cathode electrode, enabling real-time video recording of the surface deformation of the electrolyte during charging and discharging procedures, using the Proscope digital microscope (Proscope HRSCSI, Bodelin Technologies, New York, NY, USA). For strain measurement, a series of videos were recorded at a rate of 5 videos per second for a duration of 30 min/cycle. The video data acquired during both charging and discharging were subsequently transformed into TIFF frames at a frequency of 15 frames per second, facilitated by MATLAB code. Subsequently, the obtained frames were analyzed using DaVis software version 10.1.1 (LaVision, Göttingen, Germany) to determine localized strain distributions within the electrolyte across various stages of charge-discharge cycles. Concurrently, the Digital Image Correlation (DIC) technique facilitated strain measurement by tracking sequentially contrasting structures through pixel block identification within the reference image. Optimized correlation value was achieved using a subset size of 10 pixels, while step size determined the incremental displacement of each subset for successive correlation. The obtained results were temporally superimposed to visualize electrolyte deformation at distinct time points, further revealing local strain values (ε_{xx}, ε_{yy}, ε_{xy}) graphically plotted over time.

3.6. Finite element analysis

To gain deeper insights into the crack propagation and temperature dynamics within the system, the ABAQUS software developed by Dassault Systems (Dassault Systems, Pawtucket, RI) was used to conduct finite element analysis. To this end, an uncoupled thermal-electrical-mechanical simulation was executed. The initial step involved utilizing the thermal-electrical-mechanical method to scrutinize the temperature evolution within two interacting smooth cylinders. In this configuration, an interface with electrical and thermal conductive interactions is defined. The lower surface is fixed, and zero potential is attributed to it. The top surface's current density exhibits a variation ranging between 10 and -10 Am^{-2}, encompassing six cycles within the simulation timeframe. This simulation is conducted over a duration of 100 s, and the specific properties assigned to each layer are detailed in Table 2.

Subsequently, in the subsequent phase of the investigation, the temperatures obtained from the preceding step are used to conduct an explicit simulation aimed at replicating the cracking phenomenon within the NMC622 material. Herein, the NMC622 layer is conceptualized as a polycrystalline structure, where the individual grains are interconnected through cohesive interactions. The Al-LLZO layer remains consistent with the configuration utilized in the preceding simulation step.

The initiation of damage in the cohesive interaction is determined by adopting the maximum nominal stress criterion. When the contact traction stress attains equality with the corresponding contact traction stress, the damage initiation takes place. Subsequently, the propagation of the crack occurs when the energy surrounding the crack reaches the fracture energy of the system (see Fig. 3).

4. Results and discussions

4.1. Microstructure and elemental distribution of Al-LLZO electrolyte and the NMC622 electrode

The morphology of both the LLZO powder and the electrolyte was examined using scanning electron microscopy (SEM). Fig. 4a – c present SEM images of the powder, undoped LLZO sample, and doped LLZO

Table 5
The refined lattice parameters of Al-LLZO were obtained from the HighScore Plus Rietveld refinement using X-ray powder diffraction data taken at room temperature.

Name	Element	x	y	z	Biso	Occupancy	Site
LI1	Li	0.09710	0.18800	0.42440	1.3423	0.6920	96h
LI2	Li	0.37500	0.00000	0.25000	0.8685	0.3600	24d
O1	O	0.10032	0.19542	0.28170	1.0185	1.0000	96h
ZR1	Zr	0.00000	0.00000	0.00000	0.6396	0.9000	16a
LA1	La	0.12500	0.00000	0.25000	0.8290	1.0000	24c
AL1	Al	0.3750	0.0000	0.250	1.0867	0.0042	24d
AL2	Al	0.6915	0.5785	0.0865	1.0867	0.0162	96h

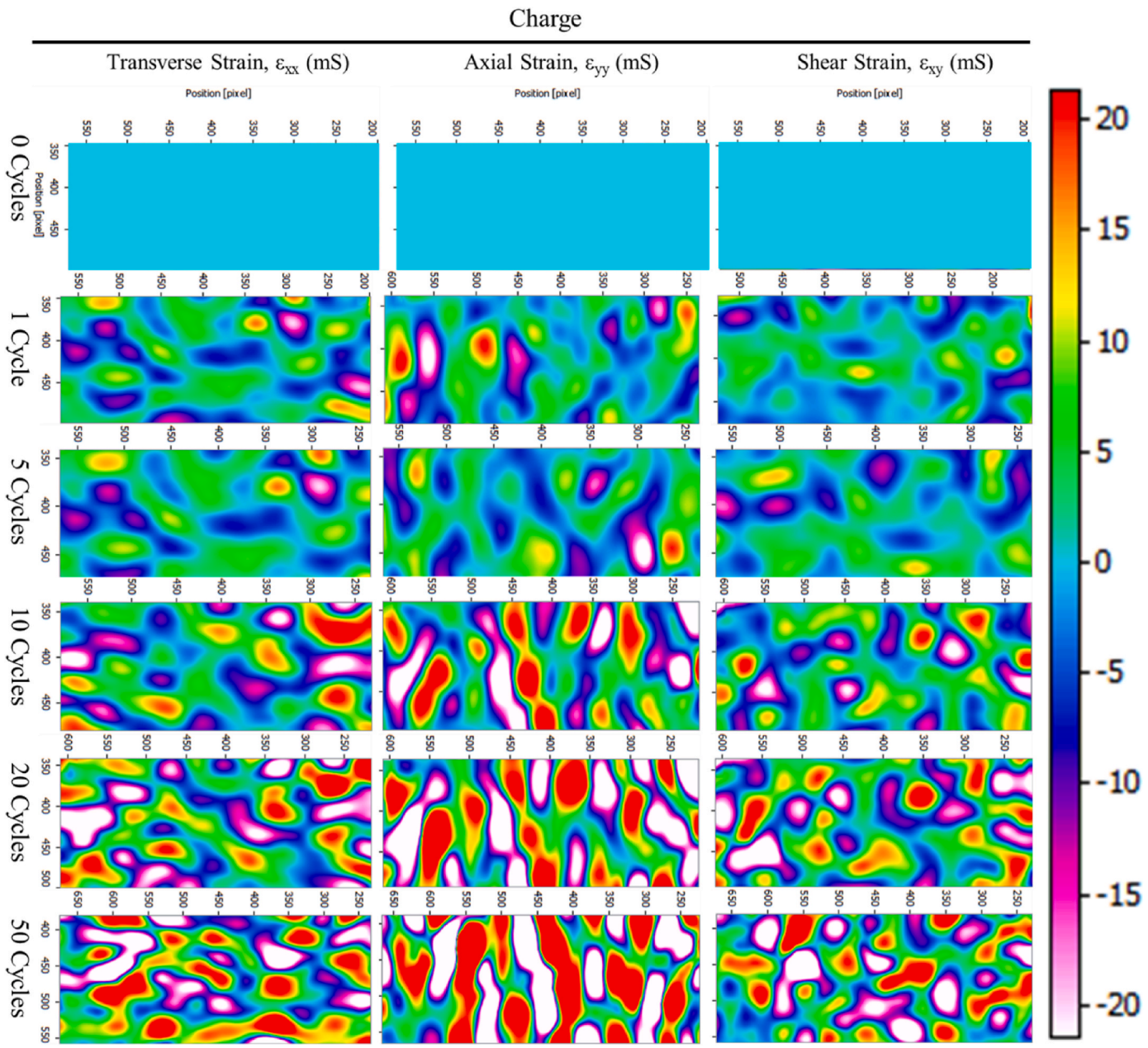

Fig. 7. Local strain distribution in the electrolyte under electrochemical cycling for 0 cycle, 1 Cycle, 5 Cycles, 10 Cycles, 20 Cycles and 50 cycles: transverse, axial and shear strains under charging.

sample, respectively. The powder product reveals a loosely distributed arrangement of agglomerated particles, characterized by irregular rounded shapes suggestive of partial compaction. The compaction rate is crucial in ceramic material processing, as insufficient compaction markedly influences the resultant density, porosity, and mechanical characteristics of the material. In the undoped samples, larger particles with surface roughness are evident, displaying considerable aggregation and lower density (see Table 3). This aggregation is likely to contribute to higher impedance and diminished ionic conductivity.

However, the Al-doped LLZO electrolytes exhibited a more compact and denser microstructure (see Table 3), devoid of cracks or pores, indicating a considerable influence of the dopant on the LLZO's microstructural properties. This structural improvement leads to reduced impedance and enhances ionic conductivity within the electrolyte. The surface roughness observed in the non-doped LLZO samples could potentially be attributed to the formation of Li_2CO_3 on the surface due to exposure to ambient air during the sample preparation for SEM analysis. Conversely, the absence of such surface layers in the Al-doped LLZO samples suggests that the dopant acts to mitigate LLZO degradation caused by CO_2 and moisture. Aluminum doping of LLZO alters the electronic structure and the surface chemistry of LLZO material [5,18]. Furthermore, the Al dopant forms a protective oxide layer on the surface of LLZO material which acts as a barrier and makes it less reactive to external species. This reduces the possibility of reaction with CO_2 and moisture [6,17,60].

Fig. 4d presents SEM image of the synthesized NMC cathode material. The image reveals a distinct and well-defined particle morphology. Additionally, some micro-pores are evident on the surface of the NMC622 electrode material.

The elemental distribution of both doped and undoped LLZO was analyzed using a scanning electron microscope with energy dispersive spectroscopy (SEM-EDS). Fig. 5a presents EDS maps of the synthesized NMC622 cathode material, demonstrating a consistent distribution of transition metal elements, albeit with notable levels of agglomeration.

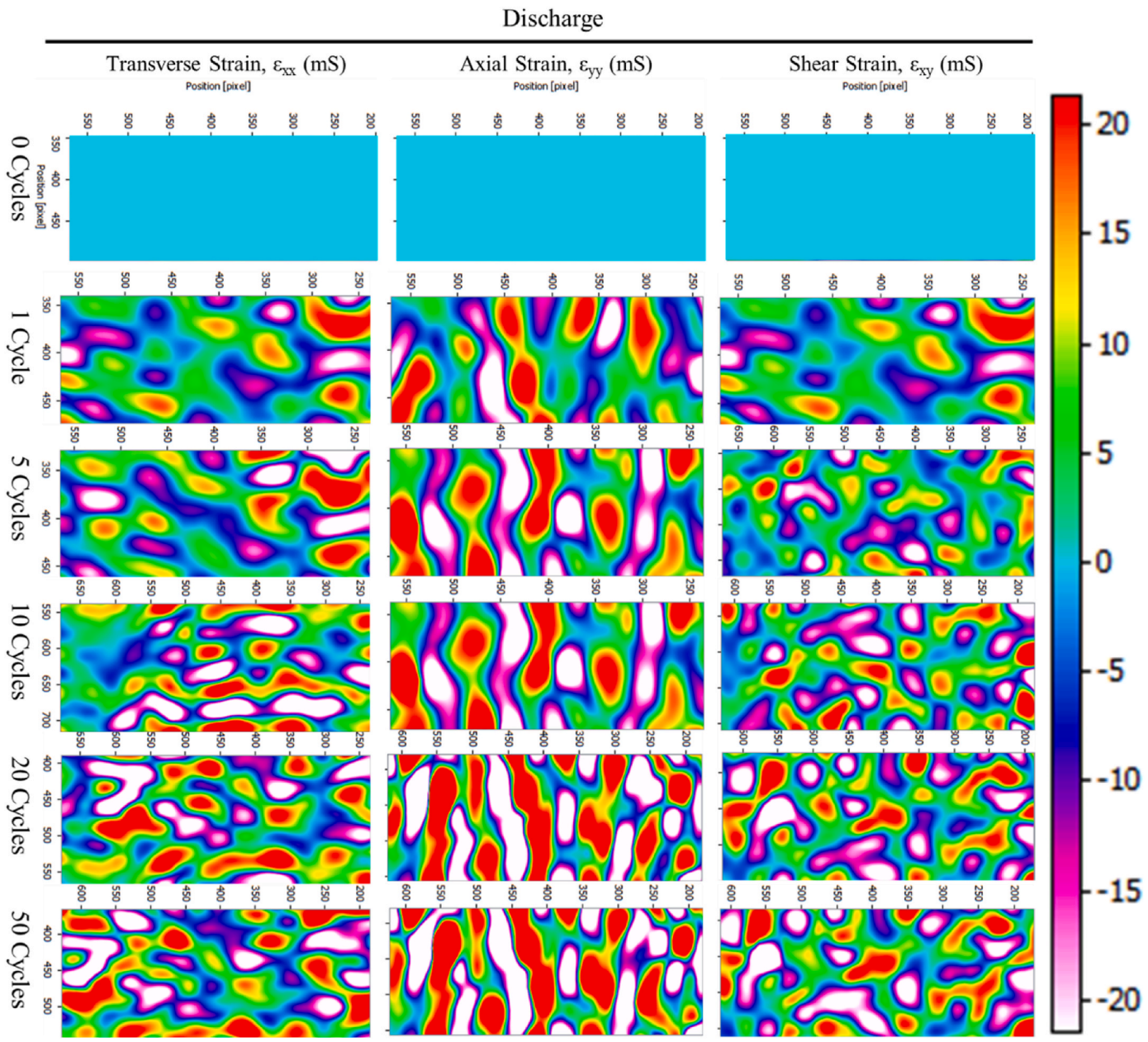

Fig. 8. Local strain distribution in the electrolyte under electrochemical cycling for 0 cycle, 1 Cycle, 5 Cycles, 10 Cycles, 20 Cycles and 50 cycles: transverse, axial and shear strains during discharging.

Fig. 5b presents SEM-EDS maps of the LLZO surface, revealing a uniform distribution of elements without evidence of agglomeration or segregation. This uniformity is attributed to the incorporation of Al atoms, which curbs Li^+ agglomeration by forming a lithium aluminate passivation layer at grain boundaries [60].

4.2. Crystalline phases and chemical composition

Fig. 6a presents the XRD patterns of both undoped and Al-doped LLZO samples annealed at 1000 °C. A comprehensive analysis was conducted using HighScore Plus Rietveld refinement software on the XRD data to accurately identify and quantify the phases present. The results show the prevalence of a cubic garnet phase, $(Li_{6.26}Al_{0.24})La_3Zr_2O_{12}$.34 %, tetragonal phase $Li_7La_3Zr_2O_{12}$.62 % and a lithium-deficient impurity phase, $La_2Zr_2O_7$ forming 4 %. Notably, the lattice constants obtained for pure LLZO are notably lower than those for Al-doped LLZO (see Table 4). This divergence is due to the facile protonation of pure LLZO during XRD measurement. Such protonation, induced by exposure to air, leads to a reaction with carbon dioxide and moisture. Consequently, the undoped LLZO undergoes a phase transition from a tetragonal to a cubic phase [5–8].

During the XRD analysis, the presence of certain impurity phases, such as Li_2CO_3, was detected at $2\theta = 32°$ due to degradation induced by air exposure. This occurrence can be attributed to side reactions leading to the formation of Li_2CO_3 and Li_2O, contributing to elevated interfacial resistance between the electrode and the electrolyte. Consequently, this limits the mobility of Li-ions, leading to a decline in battery capacity and overall performance. Additionally, the presence of Li_2ZrO_3 may contribute to the reduced peak observed at $2\theta = 21.5°$. In the context of Al-doped LLZO, the minor peak observed at $2\theta = 28.3°$ could be linked to the presence of the dilanthanum dizirconate (pyrochlore) ($La_2Zr_2O_7$) phase [5].

The X-ray diffraction (XRD) analysis of the positive electrode, NMC622, utilizing HighScore Plus software, indicated the presence of

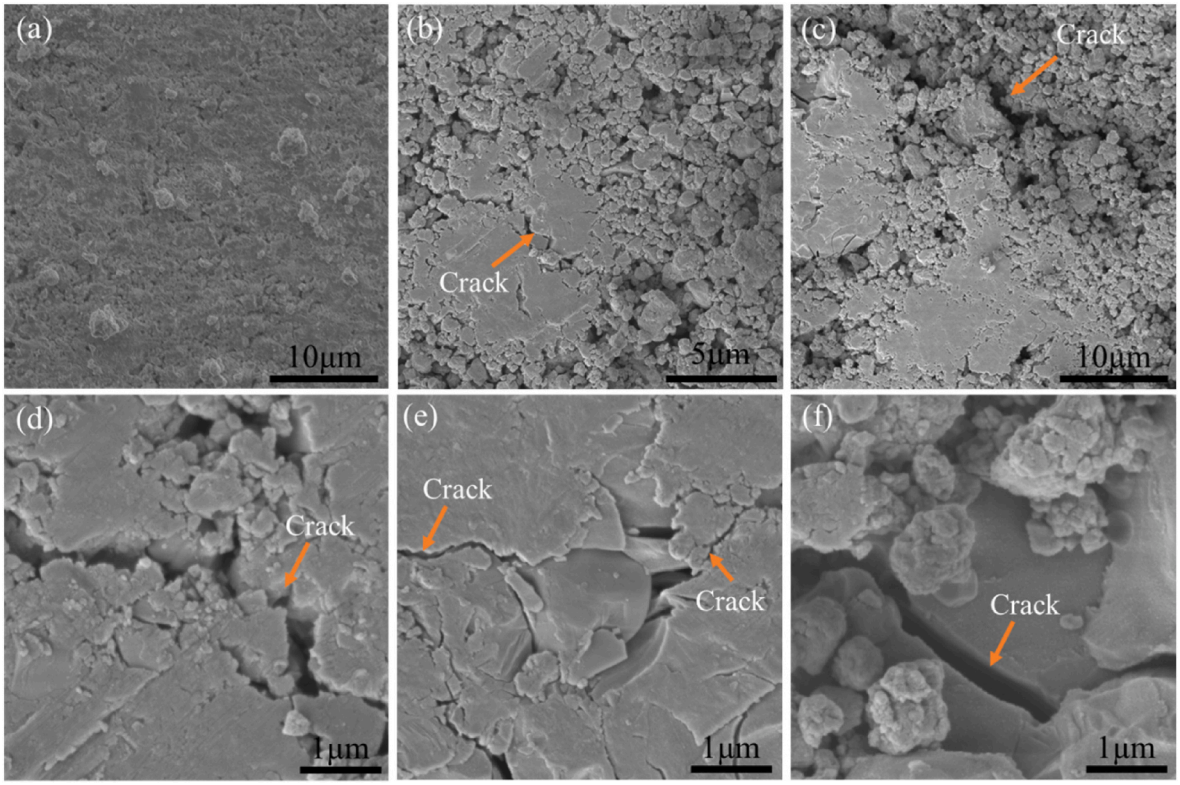

Fig. 9. SEM image of crack patterns in Al-LLZO electrolyte: (a) before cycle (b) after 5 cycles (c) after 10 cycles (d) after 20 cycles and (e) after 50 cycles.

spinel phases such as $LiCoO_2$, $Li_{0.20}Ni_2O_4$, $Li_{1.32}Mn_{1.68}O_4$, and $LiNi_{0.85}Co_{0.15}O_2$, along with their lattice constants (see Table 2 and Fig. 6b). The primary, $LiCoO_2$ phase functions as the host for lithium ions during the lithiation process, and $Li_{0.20}Ni_2O_4$ enhances the specific capacity of NMC622. Additionally, the $Li_{1.32}Mn_{1.68}O_4$ phase contributes to the thermal stability of the electrode material, while $LiNi_{0.85}Co_{0.15}O_2$ plays a role in ensuring good voltage stability, cycling stability, and high energy density for NMC622.

The Raman spectroscopy results exhibit significant peaks in the range of ~150 cm^{-1} to 550 cm^{-1}. These are attributed to the high mobility of Li^+ causing disorder in the lattice. Vibration modes between 100 cm^{-1} and 150 cm^{-1} correspond to La cation and La–O vibrations. The vibration peak at approximately 200 cm^{-1} to 450 cm^{-1} is related to the LiO_6 octahedral unit in the Li2[96h] site, confirming Li–O bond stretching in cubic LLZO (see Fig. 6d and Table 5) [61]. The presence of Al^{3+} in the 96h site of Li leads to a decrease in octahedral volume due to the smaller ionic radius of Al^{3+}. Frequency bands within the range of 300 cm^{-1} to 550 cm^{-1} are assigned to the LiO_4 tetrahedral unit in the Li1 (24d) site of cubic LLZO (see Fig. 6d and Table 5) [17,61]. A vibration band at 650 cm^{-1} indicates Zr–O bond stretching in the ZrO_6 octahedral unit [36]. Notably, the impurity peaks at around ~470 cm^{-1} and 600 cm^{-1} may be attributed to the presence of $Li_2Zr_2O_3$.

The Raman spectra shown in Fig. 6c was collected for the positive electrode, NMC622. The analysis of the Raman spectra reveals spinel phases, $LiCoO_2$, $Li_2Mn_2O_4$, $LiNiO_2$. The phases observed exhibited vibrational modes near 500-700 cm^{-1} with metal-oxide stretching modes and phonon modes near 300-500 cm^{-1}.

4.3. Strain distribution and failure mechanisms as a function charge-discharge

Figs. 7 and 8 presents the results of axial and shear strain mapping during electrochemical cycling, relative to the number of cycles. These results validate the emergence of induced strains characterized by both compressive and tensile attributes, as shown in Figs. 7 and 8, respectively. Prior to the charging process (0 cycles), the initial strains were negligible, suggesting that the residual strains were extremely small.

Nevertheless, during charging the insertion of Li-ions into the crystal structure of LLZO induces a moderate increase in strain components $(\varepsilon_{xx},\ \varepsilon_{yy},\ \varepsilon_{xy})$ as the number of cycles increased. This strain distribution is often associated with expansion or contraction of the crystal lattice due to the intercalation of lithium-ion into the LLZO crystal structure. Furthermore, the findings suggest the presence of strain partitioning in specific areas of the electrolyte, marked by both tensile and compressive axial strains (refer to Fig. 7). Substantial shear strains were also observed during the charging phase, as shown in Fig. 7.

Fig. 8 presents the strain distributions associated with discharging regime. During the discharging phase, Li-ions move from the anode to the cathode through the electrolyte. This movement involves a series of complex electrochemical processes. Furthermore, this is associated with volume change (expansion and contraction of the electrolyte crystal structure) as a result of Li-ion insertion and extraction. This phenomenon can heighten mechanical stresses and strains on the LLZO leading to intensified strain ranges. Additionally, the discharge phase can involve phase transformation or changes in the crystal structure as a result of intercalation of Li-ions into the LLZO material. Fig. 8 also shows significant increase in axial and shear strain $(\varepsilon_{xx},\ \varepsilon_{yy},\ \varepsilon_{xy})$ ranges during discharging phase. This phenomenon is attributed to the augmented deformation of the electrolyte in tandem with the growing cycle count. The reversal of ion transport direction during the discharge stage results in increased strain ranges compared to those seen during charging. This implies that both charging and discharging stages create localized strain distributions as ions move through the solid-state electrolytes between electrodes. This finding is consistent with previous research [62,63] which delineate the mechanical degradation mechanism of solid-state electrolyte materials. Hence, the derived outcomes underscore the correlation between mechanical degradation and subsequent battery failure [62].

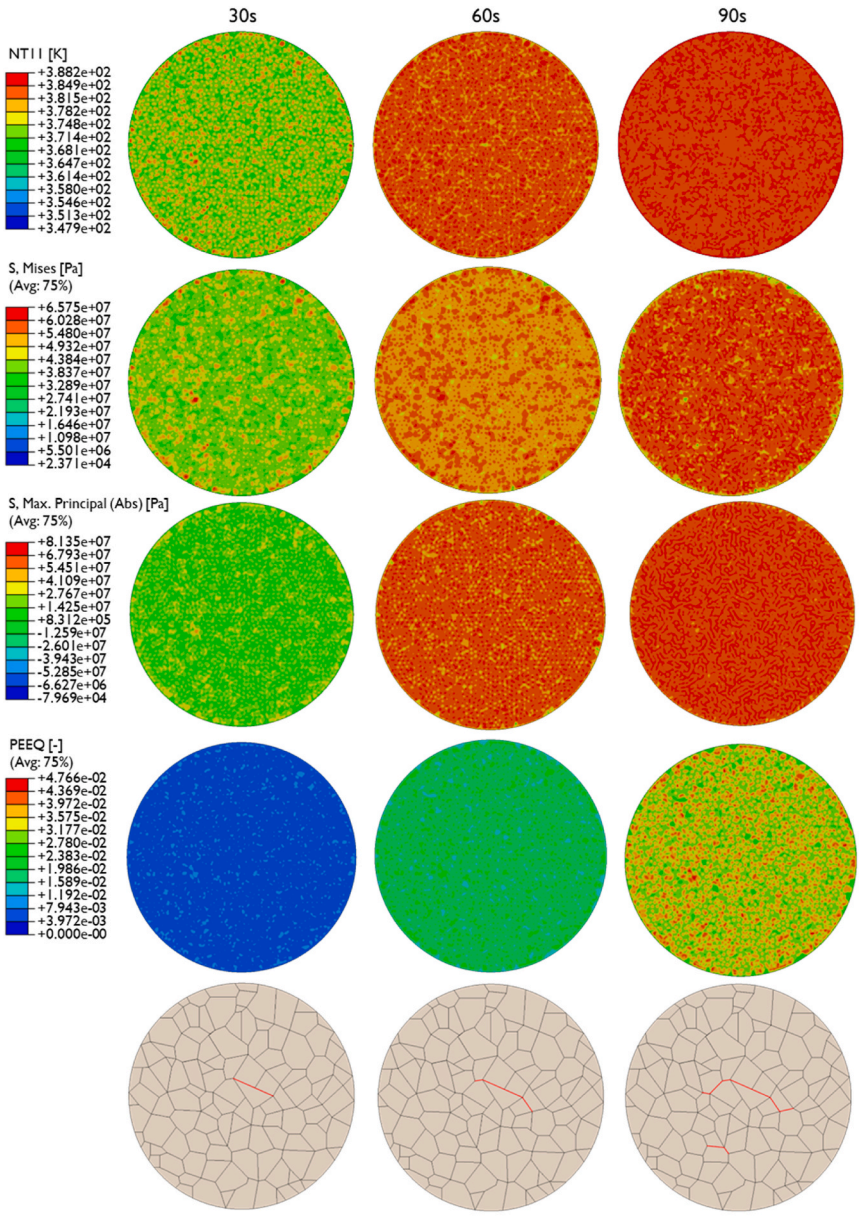

Fig. 10. (a) Temperature, von-Mises stress, max. principal stress, total strain, and crack propagation in the system from the numerical model, (b) electrical potential and temperature change in the system during the simulation time.

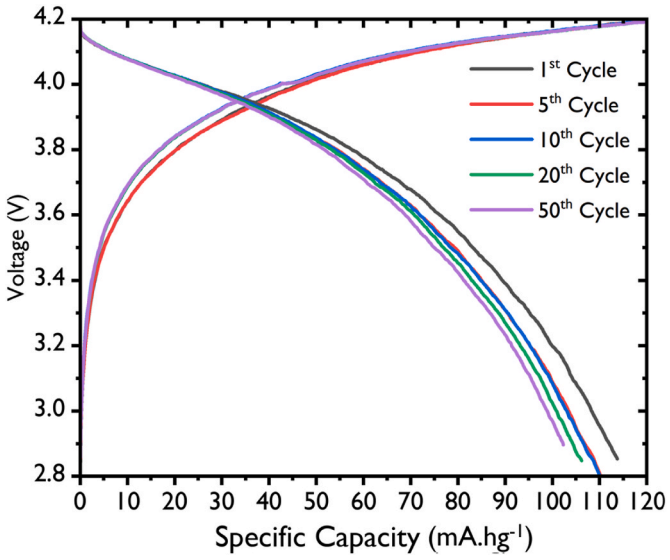

Fig. 11. Specific capacity curve for first, fifth, tenth, twentieth and fiftieth cycles.

Table 6
Summary of electrochemical performance of NMC622||Al-LLZO||Li.

No. of cycle	$R1_{bulk}$/ Ω	R2/ Ω	R3/Ω	σ/Scm^{-1}	Discharge Capacity ($mAhg^{-1}$)
0	152	1639	3126	3.04×10^{-4}	–
1	191	1647	3250	2.42×10^{-4}	115
5	218	1697	6145	2.12×10^{-4}	111
10	260	1735	7726	1.77×10^{-4}	110.5
20	279	2276	10449	1.66×10^{-4}	107.5
50	490	2558	106256	9.43×10^{-5}	102.5

Fig. 8 further illustrates the occurrence of critical levels of induced shear strain within the electrolyte during the discharge phase. Notably, the strain map for the first and fifth cycles exhibits minimal discernible disparity within the discharge phase. Conversely, as exemplified by the tenth, twentieth and fiftieth cycles, transverse, longitudinal, and shear strains become heightened. This accentuation is attributed to the alteration in the ion transfer direction, a phenomenon that triggers serious strain levels during the discharging process.

Moreover, the presence of plasticity and microcracking phenomena within specific electrolyte regions impedes effective ion transfer, consequently contributing to the accumulation of localized strain within the crystal structure of the electrolyte [62]. Furthermore, distinct plasticity becomes predominant under conditions of heightened compressive and shear strains, whereas microcracking is more prevalent within areas experiencing localized axial strains (see Fig. 8) [63]. Remarkably, the escalated distribution of local strain during the discharging phase holds the potential to induce critical damage in comparison to the charging phase, underlining the significance of strain distribution dynamics in the context of battery performance and safety.

Cracking in solid-state batteries occurs because of complex interactions involving electrochemical, mechanical, thermal, and chemical (electro-chemo-mechanical-thermal) processes during charge and discharge cycling. The electro-chemo-mechanical-thermal processes are a multifaceted interplay of factors (temperature variability, electrochemical processes, mechanical stresses, and chemical interactions) that affect the performance and the stability of batteries. This phenomenon arises because of ion movement in and out of the electrolyte during charge-discharge cycles. These processes induce significant stress and strain within the solid electrolyte material. As lithium ions move in and out of the electrolyte during charging and discharging, they induce thermal fluctuations and cause expansion and contraction of the material. This leads to mechanical stresses that can exceed the material's tolerance, resulting in localized deformations and microcracks (see Fig. 9). These cracks create pathways for the electrolyte to degrade, exposing it to chemical reactions with the electrode or ambient conditions.

Moreover, the repeated expansion and contraction cycles weaken the material's structural integrity, promoting crack propagation and further mechanical degradation. This electro-chemo-mechanical-thermal coupling leads to a feedback loop where cracks facilitate ion transport, which in turn accelerates crack propagation. This degradation mechanism undermines the overall battery performance, including reduced capacity, increased impedance, and decreased cycle life. Understanding and mitigating these interconnected processes are crucial for the design and development of robust and long-lasting solid-state batteries.

The numerical analysis delved into the mechanisms of crack nucleation and propagation within LLZO solid electrolyte, especially in response to temperature fluctuations. The simulation provides a comprehensive understanding of thermal-induced degradation mechanism in LLZO. By modeling crack initiation under varying temperature conditions, the study reveals insights into the structural behavior of LLZO and identifies conditions conducive to crack formation. As illustrated in Fig. 10, the initiation of cracks occurs at a central location within the system. Subsequently, this initial crack sets in motion a propagation process that extends until it reaches the extremities of the layer. During the progression of this crack, a secondary crack emerges at a lower point in the layer. Concurrently, the temperature profile within the system exhibits fluctuations akin to the pattern observed in the current density behavior, with an additional discernible upward ramp in the temperature trajectory. This correlation between temperature and current density dynamics underscores the intricate interplay between electro-thermo-mechanical processes governing the system's behavior.

Moreover, the modeling results establish a connection between crack nucleation and the broader phenomenon of thermal runaway, contributing to a deeper comprehension of the intricate interplay between temperature fluctuations, crack formation, and the potential risks associated with thermal instability in Li-ion battery systems.

4.4. Effect of electrochemical cycling charge-discharge on the performance of the cell

In this study, an investigation was conducted to assess the impact of charge/discharge cycles and mechanical deformations on the performance of Al-LLZO-based solid-state lithium batteries (ASSLBs) under a scan rate of 0.5C. Electrochemical cycling experiments were systematically performed to analyze the degradation characteristics and the mechanisms of capacity fading in the electrolyte due to induced strains. Illustrated in Fig. 11 is the capacity/voltage profile of the NMC622/Al-LLZO/Li cell with an upper cut-off voltage of 4.2 V, presented for the first, fifth, tenth, twentieth, and fiftieth cycles. The initial performance of the Al-LLZO-based battery, following electro-chemo-mechanical deformation at a 0.5C rate, yielded a specific discharge capacity of 115 $mAhg^{-1}$. Subsequent cycling, namely the 1st, 5th, 10th, 20th, and 50th cycles, highlighted specific discharge capacities of 115, 111.5, 110.4, 107.5, and 102.5 $mAhg^{-1}$, respectively. These results indicate a notable consistency in the cycling behavior of the cells (see Table 6).

Moreover, the findings reveal that as mechanical deformation increases, the overall charging capacity of the battery diminishes, accompanied by a shift of the charging curve towards higher voltages. This observation substantiates a gradual decrease in battery capacity, attributed to partial interfacial contact between the electrolyte and the electrode, as well as the expansion and contraction of the electrodes during charge/discharge processes. Notably, the occurrence of microcracking in the electrolyte during strain measurement under electrochemical cycling, as depicted in Fig. 9, further contributes to a significant reduction in battery capacity, thereby underscoring its

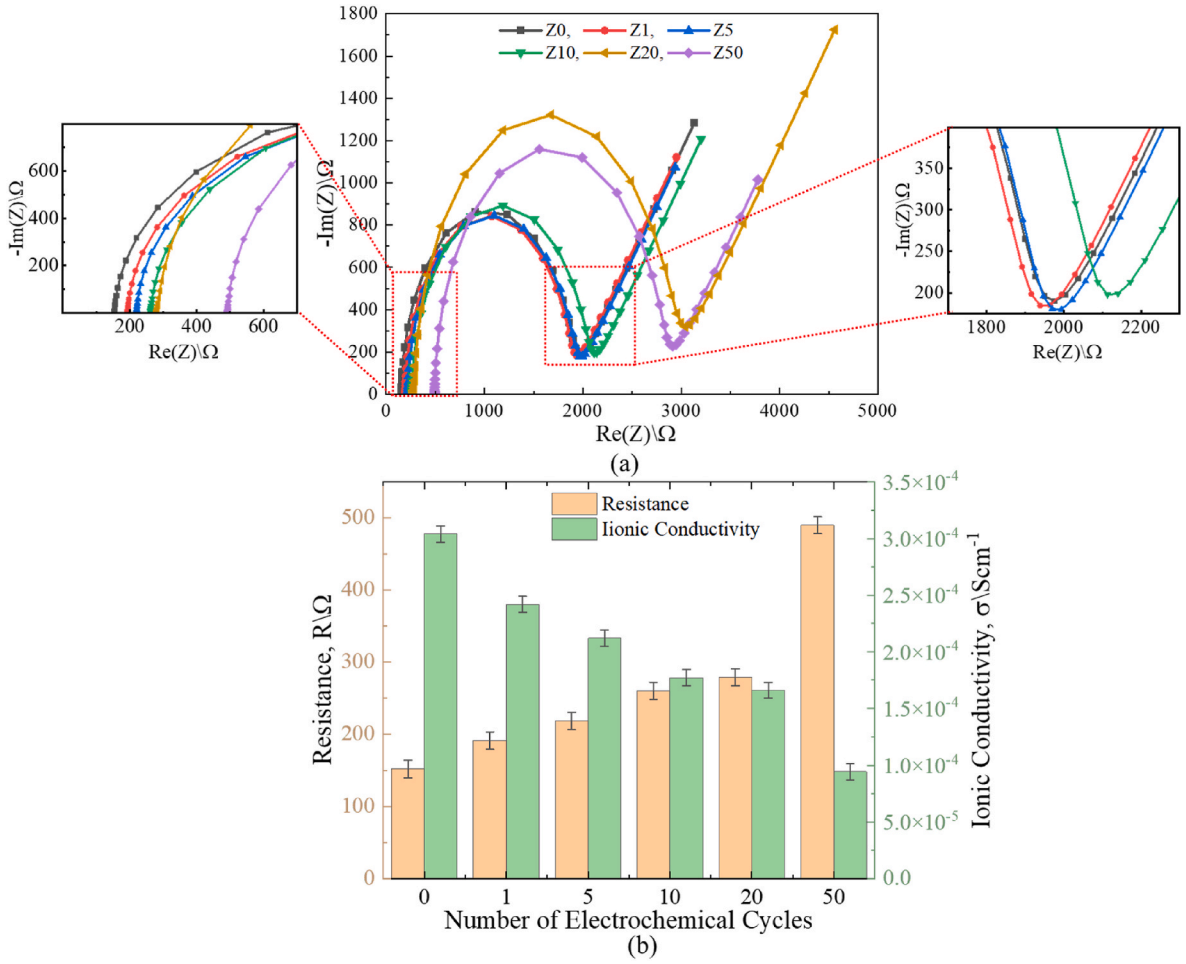

Fig. 12. (a) Nyquist plot of the impedance computed from the EIS measurement performed at room temperature, (b) Effects of electrochemical cycling on resistance and ionic conductivity.

significance within the context of this study [45].

In Fig. 12-a, the impedance spectra of the NMC622||Al-LLZO||Li cell are presented. Within this spectrum, the bulk resistance of the cell is depicted by the Nyquist arc positioned on the left side within the high-frequency region. On the right side, an additional arc emerges within the low-frequency region, indicative of the charge transfer resistance or interfacial resistance of the Al-LLZO electrolyte. Furthermore, the presence of oblique lines on the arc can be attributed to electrode polarization arising from the diffusion and electrochemical transfer of Li + at the Li-electrode interface. These characteristics are coupled with the impact of strain accumulation, leading to microcracking within the electrolyte.

4.5. Implications

The periodic migration of Li-ions through the solid electrolyte induces the evolution of strains within the material. This phenomenon arises as charges accumulate at distinct regions within the solid electrolyte. This ion movement across the solid electrolyte gives rise to spatial and temporal variations in the distribution of strains. These fluctuations in strain distribution play a pivotal role in the initiation of cyclic damage, characterized by plastic deformation and cracking processes. Notably, during the charging phase of the battery cycle, the strain distribution is comparatively lower in magnitude compared to the strains experienced during the discharging phase. The discharging stage is associated with heightened levels of cracking and plastic deformation within the solid electrolyte when contrasted with the charging phase.

Furthermore, the strain distribution on the electrolyte surface adjoining the positive electrode exhibits a predominantly tensile nature. This transitions to strains of a more compressive character in both transverse and longitudinal directions. Initially, the electrolyte surface contains a substantial concentration of Li-ions, which gradually depletes over time in response to the charging and discharging cycles. This depletion near the electrolyte surface close to the cathode is attributed to the intercalation and deintercalation mechanisms, leading to a reduction in strain values during the charging process.

In contrast, the accumulation of Li-ions near the same surface during discharging triggers reactions with entrapped oxygen in interstitial voids, causing a decline in Li-ion concentration. Consequently, there is a need to better understand the factors that lead to the spatial and temporal variations in the localized strains associated with charge-discharge cycles. There is also a need to develop life prediction tools that can be used to estimate the effects of strain accumulation on the lifetimes of Li ion batteries. These are the challenges and opportunities for future use of Li-ion batteries with LLZO electrolytes.

5. Concluding remarks

This study explores the effects of thermo-electro-chemo-mechanical coupling in all-solid-state Li metal batteries. It reveals a multifaceted interplay of factors that affect the performance and stability of these advanced energy storage systems. The intricate coupling between temperature variability, electrochemical processes, mechanical stresses, and chemical interactions is elucidated highlighting the challenges and

opportunities for designing robust all-solid-state batteries.

The current results reveal the impact of temperature gradients on Li-ion transport and interfacial behavior in the ASSBs. The effects of temperature (on electrolyte ionic conductivity and electrode reactions) are elucidated along with the effects of electrochemical cycling that results in deformation and cracking phenomena. The interplay between mechanical stresses and electrochemical processes is explored using finite element modeling that provides valuable insights into the effects of temperature and mechano-electrochemistry on battery performance. The results reveal that electrochemical cycling results in progressive deformation (induced strains and stresses), Joule heating and cracking.

The current work suggests that the failure of ASSBs occurs by the combined effects of strain evolution, heating and cracking phenomena during charging and discharging of ASSBs. This results in progressive strain accumulation that results ultimately in the degradation of battery performance. Thus, the design of robust ASSBs can be guided by finite element simulations of charging and discharging cycles that give rise to stress/strain evolution and cracking phenomena. This can pave the way for the development of higher-performance ASSB technologies.

CRediT authorship contribution statement

John Adjah: Conceptualization, Data curation, Formal analysis, Investigation, Methodology, Project administration, Software, Validation, Visualization, Writing – original draft, Writing – review & editing. **Kingsley I. Orisekeh:** Project administration, Writing – review & editing. **Ridwan A. Ahmed:** Formal analysis, Project administration, Writing – review & editing. **Mobin Vandadi:** Software, Visualization, Writing – original draft, Writing – review & editing. **Benjamin Agyei-Tuffour:** Conceptualization, Formal analysis, Resources, Supervision, Writing – review & editing. **Emmanuel Nyankson:** Supervision, Writing – review & editing, Supervision, Writing – review & editing. **Joseph Asare:** Supervision, Writing – review & editing. **Nima Rahbar:** Resources, Software, Supervision, Writing – review & editing. **Winston O. Soboyejo:** Conceptualization, Formal analysis, Funding acquisition, Resources, Software, Supervision, Writing – original draft, Writing – review & editing.

Declaration of competing interest

The authors declare that they have no known competing financial interests or personal relationships that could have appeared to influence the work reported in this paper.

Data availability

Data will be made available on request.

Acknowledgment

The technical and financial support from the Global Fund from the Worcester Polytechnic Institute is acknowledged. The contribution and incisive discussions from experts from the SUNY Polytechnic Institute is also greatly acknowledged. Support from the University of Ghana through the BANGA-Africa program is also rightly acknowledged.

Appendix A. Supplementary data

Supplementary data to this article can be found online at https://doi.org/10.1016/j.jpowsour.2023.234022.

References

[1] B. Nykvist, F. Sprei, M. Nilsson, Assessing the progress toward lower priced long range battery electric vehicles, Energy Pol. 124 (2019) 144–155, https://doi.org/10.1016/j.enpol.2018.09.035.

[2] Y.K. Sun, Promising all-solid-state batteries for future electric vehicles, ACS Energy Lett. 5 (2020) 3221–3223, https://doi.org/10.1021/acsenergylett.0c01977.

[3] B. Nykvist, M. Nilsson, Rapidly falling costs of battery packs for electric vehicles, Nat. Clim. Change 5 (2015) 329–332, https://doi.org/10.1038/nclimate2564.

[4] M. Waseem, M. Ahmad, A. Parveen, M. Suhaib, Battery technologies and functionality of battery management system for EVs: current status, key challenges, and future prospectives, J. Power Sources 580 (2023), https://doi.org/10.1016/j.jpowsour.2023.233349.

[5] J. Sastre, A. Priebe, M. Döbeli, J. Michler, A.N. Tiwari, Y.E. Romanyuk, Lithium garnet Li7La3Zr2O12 electrolyte for all-solid-state batteries: closing the gap between bulk and thin film Li-ion conductivities, Adv. Mater. Interfac. 7 (2020), https://doi.org/10.1002/admi.202000425.

[6] C.A. Geiger, E. Alekseev, B. Lazic, M. Fisch, T. Armbruster, R. Langner, M. Fechtelkord, N. Kim, T. Pettke, W. Weppner, Crystal chemistry and stability of "Li7La 3Zr2O12" garnet: a fast lithium-ion conductor, Inorg. Chem. 50 (2011) 1089–1097, https://doi.org/10.1021/ic101914e.

[7] R. Murugan, V. Thangadurai, W. Weppner, Fast lithium ion conduction in garnet-type Li7La 3Zr2O12, Angew. Chem. Int. Ed. 46 (2007) 7778–7781, https://doi.org/10.1002/anie.200701144.

[8] V. Thangadurai, H. Kaack, W.J.F. Weppner, Novel fast lithium ion conduction in garnet-type Li5La3M2O12 (M = Nb, Ta), J. Am. Ceram. Soc. 86 (2003) 437–440, https://doi.org/10.1111/j.1151-2916.2003.tb03318.x.

[9] J.A. Lewis, J. Tippens, F. Javier, Q. Cortes, M.T. Mcdowell, Chemo-Mechanical Challenges in Solid-State Batteries, 2019.

[10] P. Ping, Q. Wang, P. Huang, J. Sun, C. Chen, Thermal behaviour analysis of lithium-ion battery at elevated temperature using deconvolution method, Appl. Energy 129 (2014) 261–273, https://doi.org/10.1016/j.apenergy.2014.04.092.

[11] E. Peled, S. Menkin, Review—sei: past, present and future, J. Electrochem. Soc. 164 (2017) A1703–A1719, https://doi.org/10.1149/2.1441707jes.

[12] K.M. Abraham, Chemical and Electrochemical Processes in Some Lithium-Liquid Cathode Batteries*, 1991.

[13] S. Randau, D.A. Weber, O. Kötz, R. Koerver, P. Braun, A. Weber, E. Ivers-Tiffée, T. Adermann, J. Kulisch, W.G. Zeier, F.H. Richter, J. Janek, Benchmarking the performance of all-solid-state lithium batteries, Nat. Energy 5 (2020) 259–270, https://doi.org/10.1038/s41560-020-0565-1.

[14] J.B. Goodenough, K.S. Park, The Li-ion rechargeable battery: a perspective, J. Am. Chem. Soc. 135 (2013) 1167–1176, https://doi.org/10.1021/ja3091438.

[15] J.B. Goodenough, K.-S. Park, ChemInform abstract: the Li-ion rechargeable battery: a perspective, ChemInform 44 (2013), https://doi.org/10.1002/chin.201320273.

[16] H. Xu, Y. Li, A. Zhou, N. Wu, S. Xin, Z. Li, J.B. Goodenough, Li3N-Modified garnet electrolyte for all-solid-state lithium metal batteries operated at 40 °c, Nano Lett. 18 (2018) 7414–7418, https://doi.org/10.1021/acs.nanolett.8b03902.

[17] T. Thompson, J. Wolfenstine, J.L. Allen, M. Johannes, A. Huq, I.N. David, J. Sakamoto, Tetragonal vs. cubic phase stability in Al-free Ta doped Li 7La3Zr2O12 (LLZO), J Mater Chem A Mater 2 (2014) 13431–13436, https://doi.org/10.1039/c4ta02099e.

[18] M.M. Raju, F. Altayran, M. Johnson, D. Wang, Q. Zhang, Crystal structure and preparation of Li7La3Zr2O12 (LLZO) solid-state electrolyte and doping impacts on the conductivity: an overview, Electrochemistry (Tokyo, Jpn.) 2 (2021) 390–414, https://doi.org/10.3390/electrochem2030026.

[19] M.M. Raju, F. Altayran, M. Johnson, D. Wang, Q. Zhang, Crystal structure and preparation of Li7La3Zr2O12 (LLZO) solid-state electrolyte and doping impacts on the conductivity: an overview, Electrochemistry (Tokyo, Jpn.) 2 (2021) 390–414, https://doi.org/10.3390/electrochem2030026.

[20] Z. Ding, J. Li, J. Li, C. An, Review—Interfaces, Key issue to Be solved for all solid-state lithium battery technologies, J. Electrochem. Soc. 167 (2020), 070541, https://doi.org/10.1149/1945-7111/ab7f84.

[21] Q.H. Nguyen, V.T. Luu, H.L. Nguyen, Y.W. Lee, Y. Cho, S.Y. Kim, Y.S. Jun, W. Ahn, Li7La3Zr2O12 garnet solid polymer electrolyte for highly stable all-solid-state batteries, Front. Chem. 8 (2021), https://doi.org/10.3389/fchem.2020.619832.

[22] R. Chen, A.M. Nolan, J. Lu, J. Wang, X. Yu, Y. Mo, L. Chen, X. Huang, H. Li, The thermal stability of lithium solid electrolytes with metallic lithium, Joule 4 (2020) 812–821, https://doi.org/10.1016/j.joule.2020.03.012.

[23] T. Deng, G. Zhang, Y. Ran, Study on thermal management of rectangular Li-ion battery with serpentine-channel cold plate, Int. J. Heat Mass Tran. 125 (2018) 143–152, https://doi.org/10.1016/j.ijheatmasstransfer.2018.04.065.

[24] Z. Sun, M. Li, B. Xiao, X. Liu, H. Lin, B. Jiang, H. Liu, M. Li, D.L. Peng, Q. Zhang, In situ transmission electron microscopy for understanding materials and interfaces challenges in all-solid-state lithium batteries, ETransportation 14 (2022), https://doi.org/10.1016/j.etran.2022.100203.

[25] L. Huang, T. Lu, G. Xu, X. Zhang, Z. Jiang, Z. Zhang, Y. Wang, P. Han, G. Cui, L. Chen, Thermal runaway routes of large-format lithium-sulfur pouch cell batteries, Joule 6 (2022) 906–922, https://doi.org/10.1016/j.joule.2022.02.015.

[26] N. Johnson, P. Albertus, Modeling thermal behavior and safety of large format all-solid-state lithium metal batteries under thermal ramp and short circuit conditions, J. Electrochem. Soc. 169 (2022), 060546, https://doi.org/10.1149/1945-7111/ac79cf.

[27] K. Parascos, J.L. Watts, J.A. Alarco, Y. Chen, P.C. Talbot, Compositional and structural control in LLZO solid electrolytes, RSC Adv. 12 (2022) 23466–23480, https://doi.org/10.1039/d2ra03303h.

[28] Z. An, K. Shah, L. Jia, Y. Ma, A parametric study for optimization of minichannel based battery thermal management system, Appl. Therm. Eng. 154 (2019) 593–601, https://doi.org/10.1016/j.applthermaleng.2019.02.088.

[29] T. Deng, G. Zhang, Y. Ran, Study on thermal management of rectangular Li-ion battery with serpentine-channel cold plate, Int. J. Heat Mass Tran. 125 (2018) 143–152, https://doi.org/10.1016/j.ijheatmasstransfer.2018.04.065.

[30] G. Argandoña, M. Aresti, J.M. Blanco, E. Muel, J. Esarte, Li2co3 as protection for a high-temperature thermoelectric generator: thermal stability and corrosion analysis, Appl. Sci. (2021) 11, https://doi.org/10.3390/app11167597.
[31] Y. Chen, E. Rangasamy, C.R. Dela Cruz, C. Liang, K. An, A study of suppressed formation of low-conductivity phases in doped Li7La3Zr2O12 garnets by in situ neutron diffraction, J Mater Chem A Mater 3 (2015) 22868–22876, https://doi.org/10.1039/c5ta04902d.
[32] J. Tippens, J.C. Miers, A. Afshar, J.A. Lewis, F.J.Q. Cortes, H. Qiao, T.S. Marchese, C.V. Di Leo, C. Saldana, M.T. McDowell, Visualizing chemomechanical degradation of a solid-state battery electrolyte, ACS Energy Lett. 4 (2019) 1475–1483, https://doi.org/10.1021/acsenergylett.9b00816.
[33] D. Bistri, C.V. Di Leo, A continuum electro-chemo-mechanical gradient theory coupled with damage: application to Li-metal filament growth in all-solid-state batteries, J. Mech. Phys. Solid. 174 (2023), https://doi.org/10.1016/j.jmps.2023.105252.
[34] W. Zhang, F.H. Richter, S.P. Culver, T. Leichtweiss, J.G. Lozano, C. Dietrich, P. G. Bruce, W.G. Zeier, J. Janek, Degradation mechanisms at the Li10GeP2S12/LiCoO2 cathode interface in an all-solid-state lithium-ion battery, ACS Appl. Mater. Interfaces 10 (2018) 22226–22236, https://doi.org/10.1021/acsami.8b05132.
[35] G. Bucci, T. Swamy, Y.M. Chiang, W.C. Carter, Modeling of internal mechanical failure of all-solid-state batteries during electrochemical cycling, and implications for battery design, J Mater Chem A Mater 5 (2017) 19422–19430, https://doi.org/10.1039/c7ta03199h.
[36] C. Chen, Y. Sun, L. He, M. Kotobuki, E. Hanc, Y. Chen, K. Zeng, L. Lu, Microstructural and electrochemical properties of Al- and Ga-doped Li7La3Zr2O12 garnet solid electrolytes, ACS Appl. Energy Mater. 3 (2020) 4708–4719, https://doi.org/10.1021/acsaem.0c00347.
[37] R. Chen, A.M. Nolan, J. Lu, J. Wang, X. Yu, Y. Mo, L. Chen, X. Huang, H. Li, The thermal stability of lithium solid electrolytes with metallic lithium, Joule 4 (2020) 812–821, https://doi.org/10.1016/j.joule.2020.03.012.
[38] R.C. Massé, C. Liu, Y. Li, L. Mai, G. Cao, Energy storage through intercalation reactions: electrodes for rechargeable batteries, Natl. Sci. Rev. 4 (2017) 26–53, https://doi.org/10.1093/nsr/nww093.
[39] P.K. Nayak, L. Yang, W. Brehm, P. Adelhelm, Von Lithium- zu Natriumionenbatterien: vorteile, Herausforderungen und Überraschendes, Angew. Chem. 130 (2018) 106–126, https://doi.org/10.1002/ange.201703772.
[40] M.D. Bhatt, C. O'Dwyer, Recent progress in theoretical and computational investigations of Li-ion battery materials and electrolytes, Phys. Chem. Chem. Phys. 17 (2015) 4799–4844, https://doi.org/10.1039/c4cp05552g.
[41] S. Panchal, M. Mathew, R. Fraser, M. Fowler, Electrochemical thermal modeling, and experimental measurements of 18650 cylindrical lithium-ion battery during discharge cycle for an EV, Appl. Therm. Eng. 135 (2018) 123–132, https://doi.org/10.1016/j.applthermaleng.2018.02.046.
[42] D. Danilov, R.A.H. Niessen, P.H.L. Notten, Modeling all-solid-state Li-ion batteries, J. Electrochem. Soc. 158 (2011) A215, https://doi.org/10.1149/1.3521414.
[43] N. Kazemi, D.L. Danilov, L. Haverkate, N.J. Dudney, S. Unnikrishnan, P.H. L. Notten, Modeling of all-solid-state thin-film Li-ion batteries: accuracy improvement, Solid State Ionics 334 (2019) 111–116, https://doi.org/10.1016/j.ssi.2019.02.003.
[44] P.K. Nayak, L. Yang, W. Brehm, P. Adelhelm, Von Lithium- zu Natriumionenbatterien: vorteile, Herausforderungen und Überraschendes, Angew. Chem. 130 (2018) 106–126, https://doi.org/10.1002/ange.201703772.
[45] J.S. Edge, S. O'Kane, R. Prosser, N.D. Kirkaldy, A.N. Patel, A. Hales, A. Ghosh, W. Ai, J. Chen, J. Yang, S. Li, M.C. Pang, L. Bravo Diaz, A. Tomaszewska, M. W. Marzook, K.N. Radhakrishnan, H. Wang, Y. Patel, B. Wu, G.J. Offer, Lithium ion battery degradation: what you need to know, Phys. Chem. Chem. Phys. 23 (2021) 8200–8221, https://doi.org/10.1039/d1cp00359c.
[46] S. Masanta, C. Nayak, S. Maitra, S. Rudra, D. Chowdhury, S. Raha, M. Pradhan, B. Satpati, P. Pal, A. Singha, Engineering multifunctionality in MoSe2 nanostructures via strategic Mn doping for electrochemical energy storage and photosensing, ACS Appl. Nano Mater. (2022), https://doi.org/10.1021/acsanm.2c05592.
[47] Y. Gong, K. Fu, S. Xu, J. Dai, T.R. Hamann, L. Zhang, G.T. Hitz, Z. Fu, Z. Ma, D. W. McOwen, X. Han, L. Hu, E.D. Wachsman, Lithium-ion conductive ceramic textile: a new architecture for flexible solid-state lithium metal batteries, Mater. Today 21 (2018), https://doi.org/10.1016/j.mattod.2018.01.001.
[48] H. Jiang, Y. Wu, J. Ma, Y. Liu, L. Wang, X. Yao, H. Xiang, Ultrathin polymer-in-ceramic and ceramic-in-polymer bilayer composite solid electrolyte membrane for high-voltage lithium metal batteries, J. Membr. Sci. 640 (2021), https://doi.org/10.1016/j.memsci.2021.119840.
[49] D. Aleksandrov, P. Novikov, A. Popovich, Q. Wang, Superionic solid electrolyte Li7 La3 Zr2 O12 synthesis and thermodynamics for application in all-solid-state lithium-ion batteries, Materials 15 (2022), https://doi.org/10.3390/ma15010281.
[50] W. Xue, Y. Yang, Q. Yang, Y. Liu, L. Wang, C. Chen, R. Cheng, The effect of sintering process on lithium ionic conductivity of Li6.4Al0.2La3Zr2O12 garnet produced by solid-state synthesis, RSC Adv. 8 (2018) 13083–13088, https://doi.org/10.1039/c8ra01329b.
[51] M.J. Lee, D.O. Shin, J.Y. Kim, J. Oh, S.H. Kang, J. Kim, K.M. Kim, Y.M. Lee, S. O. Kim, Y.G. Lee, Interfacial barrier free organic-inorganic hybrid electrolytes for solid state batteries, Energy Storage Mater. 37 (2021) 306–314, https://doi.org/10.1016/j.ensm.2021.02.013.
[52] R. Bock, M. Onsrud, H. Karoliussen, B.G. Pollet, F. Seland, O.S. Burheim, Thermal gradients with sintered solid state electrolytes in lithium-ion batteries, Energies 13 (2020), https://doi.org/10.3390/en13010253.
[53] A.A. Hubaud, D.J. Schroeder, B.J. Ingram, J.S. Okasinski, J.T. Vaughey, Thermal expansion in the garnet-type solid electrolyte (Li7-xAlx/3)La3Zr2O12 as a function of Al content, J. Alloys Compd. 644 (2015) 804–807, https://doi.org/10.1016/j.jallcom.2015.05.067.
[54] S. Maeng, Y. Chung, S. Min, Y. Shin, Enhanced mechanical strength and electrochemical performance of core–shell structured high–nickel cathode material, J. Power Sources 448 (2020), https://doi.org/10.1016/j.jpowsour.2019.227395.
[55] A. Celen, O. Kalkan, Numerical investigation on the usage of finned surface in lithium nickel manganese cobalt oxides batteries by using air cooling method, Energy Storage 3 (2021), https://doi.org/10.1002/est2.216.
[56] K. Smith, C.Y. Wang, Solid-state diffusion limitations on pulse operation of a lithium ion cell for hybrid electric vehicles, J. Power Sources 161 (2006) 628–639, https://doi.org/10.1016/j.jpowsour.2006.03.050.
[57] M.Z. Yar, M. Khalid, M. Yasin, K. Naz, M.G. Bahar Ashiq, M. Younas, Hammad, T. Alshahrani, K.I. Hussein, K. Bin Hassan, B. Ahmed, M.M. Javid, Structural, dielectric, and magnetic properties of nickel rich manganese substituted Li2Ni6MnxCo2-xO10 nanomaterial synthesized via sol-gel method, Phys. B Condens. Matter 666 (2023), 415069, https://doi.org/10.1016/j.physb.2023.415069.
[58] M. Steinhardt, E.I. Gillich, A. Rheinfeld, L. Kraft, M. Spielbauer, O. Bohlen, A. Jossen, Low-effort determination of heat capacity and thermal conductivity for cylindrical 18650 and 21700 lithium-ion cells, J. Energy Storage 42 (2021), https://doi.org/10.1016/j.est.2021.103065.
[59] F.B. Spingler, W. Wittmann, J. Sturm, B. Rieger, A. Jossen, Optimum fast charging of lithium-ion pouch cells based on local volume expansion criteria, J. Power Sources 393 (2018) 152–160, https://doi.org/10.1016/j.jpowsour.2018.04.095.
[60] H. El-Shinawi, G.W. Paterson, D.A. MacLaren, E.J. Cussen, S.A. Corr, Low-temperature densification of Al-doped Li7La3Zr2O12: a reliable and controllable synthesis of fast-ion conducting garnets, J Mater Chem A Mater 5 (2017) 319–329, https://doi.org/10.1039/c6ta06961d.
[61] F. Tietz, T. Wegener, M.T. Gerhards, M. Giarola, G. Mariotto, Synthesis and Raman micro-spectroscopy investigation of Li7La3Zr2O12, Solid State Ionics 230 (2013) 77–82, https://doi.org/10.1016/j.ssi.2012.10.021.
[62] L. Li, X. Chen, Q. Yuan, T. Wang, H. Ji, S. Papović, K. Raleva, F. Pan, T. Yang, J. Li, Effects of minor mechanical deformation on the lifetime and performance of commercial 21700 lithium-ion battery, J. Electrochem. Soc. 169 (2022), https://doi.org/10.1149/1945-7111/ac79d4.
[63] N. Ebechidi, R. Ahmed, O. Oyewole, A. Bello, P. Ngene, W. Soboyejo, Charge-discharge-induced local strain distributions in a lithium amide-borohydride-iodide [LiBH4-LiNH2-LiI] solid electrolyte, J. Energy Storage 47 (2022), https://doi.org/10.1016/j.est.2021.103600.